The Origin of Persistently Nonthermal Solar Wind Electrons: the Steady Electron Runaway Model's Demonstration of Dreicer Bifurcation using Measured $E_\parallel$ and Ion–Electron Coulomb Drag

Jack D. Scudder[1,2]

[1] Space Science Institute, Boulder, CO 80301, USA; jscudder@spacescience.org
[2] University of Iowa, Iowa City, IA 52242, USA

Abstract

The Steady Electron Runaway Model (SERM) develops the hypothesis that the solar wind's observed ubiquitous nonthermal electron velocity distribution functions (eVDFs) are caused by Dreicer's velocity space bifurcation in the strong dimensionless $\mathbb{E}_\parallel$ required by quasi-neutrality. SERM's predicted partitions for the pressure and density are contrasted with appropriately adapted eVDF properties from the Wind 3DP experiment (1995–1998), based on in situ observations of $\mathbb{E}_\parallel$. The observed number fraction of electrons in runaway, δ^{3DP}, follows a thousandfold decline of Dreicer's predicted fraction, δ, across the observed tenfold reduction of $\mathbb{E}_\parallel$, satisfying $\delta^{3DP} \simeq \delta^{0.89}$. SERM's predictions are shown to reproduce the observed variations with $\mathbb{E}_\parallel$ of the electron partial pressure and excess kurtosis, $\mathcal{K}_e$. $\mathcal{K}_e$ and $\mathbb{E}_\parallel$ are positively correlated across 4 yr, as expected by the SERM–Dreicer origin of the suprathermals. SERM quantitatively explains the observed 50 yr anticorrelation between δ^{3DP} and the partition slope temperature ratios. This documentation quantitatively establishes Coulomb runaway physics as the missing determinant of the ubiquitous nonthermal solar wind eVDF. Astrophysical plasmas, like stellar winds, are unavoidably inhomogeneous, requiring $\mathbb{E}_\parallel$ to enforce quasi-neutrality. Between the stars $\mathbb{E}_\parallel$ is expected to be sufficiently large that measurable runaway density fractions (0.1%–30%) will occur, producing widespread leptokurtic eVDFs. Using inhomogeneous two-fluid information, SERM predicts spatially dependent leptokurtic eVDF profiles consonant with Coulomb collisions and the fluid's $E_\parallel(r)$. SERM can also comment on its eVDFs' consistency with Maxwellians presumed in the Spitzer–Härm closure. The solar wind profile shows the implied strong radial gradient of the plasma eVDF's transformation from near thermal to strongly leptokurtic across 1.5–6 $R_\odot$.

Unified Astronomy Thesaurus concepts: Solar wind (1534); Space plasmas (1544); Collisional processes (2286)

1. Introduction

Since 1968 solar wind electrons have been ubiquitously observed to be nonthermal between a few solar radii and 10 au. The observed even moments of density and pressure are essentially replicated by a superposition of one thermal and one nonthermal subcomponent in the modeling, usually modeled by a cooler but denser convected bi-Maxwellian and hotter and much sparser convecting bi-kappa distributions. The nonthermal electron velocity distribution functions (eVDFs) across all kinetic energies have a remarkably reproducible velocity space dependence, as indicated by successful multiyear catalogs of their component properties based on such routine fits that agree with their model-independent moments through the heat flux (e.g., Salem et al. 2021). Further, these same velocity-space-modeled forms have been in essentially constant use since their introduction for electrons by Montgomery et al. (1968).

Many espouse the suggestion by Parker (1958) that nonthermal effects in the solar plasma are surely the products of some form of turbulence. The author is unaware of any successful attempts that quantitatively explain (i) how waves and turbulence ubiquitously and quantitatively produce the observed, "omnipresent," nonthermal solar wind eVDF; nor (ii) the origin of its well-documented shape properties.

The present paper explores the ideas of the Steady Electron Runaway Model (SERM; Scudder 2019c) by quantitatively documenting the prediction of nearly all the eVDF properties ubiquitously observed over the past 50 yr in the solar wind *without* adopting Parker's suggestion. The recent proponents of the turbulence interpretation are encouraged to develop ubiquitous and quantitative evidence that predicts the observed solar wind eVDF phenomena. Until then there appears no objective basis for the author to "reiterate the role played by wave fluctuations in the generation and maintenance of suprathermal populations." Despite the possible existence of such an unreported wave explanation, it is difficult to prefer presently unquantified wave explanations to quantified SERM explanations for the cause of the well-cataloged ubiquitous nonthermal solar wind eVDF.

This paper quantitatively tests that this ubiquitous suprathermal solar wind eVDF behavior should occur for any inhomogeneous plasma containing a steady $E_\parallel$, where the speed dependence of Coulomb collisions is respected and Dreicer's dimensionless electric field $\mathbb{E}_\parallel$ is not *too* large.

The SERM argument (Scudder 2019c) was motivated by (i) Dreicer's (1959, 1960) work concerning plasma runaway in laboratory plasmas; (ii) initial kinetic calculations of the 1 au eVDF by Scudder & Olbert (1979a, 1979b); and (iii) earlier empirical studies using reported and inferred temperature gradients about the size of $\mathbb{E}_\parallel$ (Scudder 1996).

SERM produces a model nonthermal eVDF compatible with assumed $\mathbb{E}_\parallel$, runaway signatures, and quasi-neutrality; the

even moment controlling shape parameters of the eVDF were predicted to be organized by $\mathbb{E}_\parallel$, the local pressure P_e, and density n_e. The runaway density fraction δ and ratio of subcomponent slope temperatures τ^2 were argued to be monotonic functions solely of $\mathbb{E}_\parallel$.

A new quantitative phase is now possible to test SERM predictions versus the observations for δ, τ, and $\mathcal{K}_e$ for each eVDF acquired by the Wind 3DP investigation (Lin et al. 1995) over a 4 yr period (1995–1998). Rather than estimating or inferring the size of $\mathbb{E}_\parallel$ asynchronously from other spacecraft spatial profiles, a *direct* method has been developed and validated that determines $E_\parallel \simeq \mathcal{O}(10^{-10})\,V/m$ and $\mathbb{E}_\parallel$ for this purpose at the time resolution of each eVDF acquisition (Scudder 2022a).

These initial SERM-I shape predictions have been augmented in the updated SERM-II model by including a statistically determined break-point energy in the SERM-II eVDF; it appears to allow for a transition zone between initial and assimilated runaways in the energy spectrum. These comparisons produce nearly perfect agreements with theoretical predictions, knowing only the size of $\mathbb{E}_\parallel$ for each eVDF.

After this introduction this paper proceeds to (i) review Dreicer's seminal insight about the velocity space bifurcation; (ii) illustrate the model-independent observed positive correlation of the Wind 3DP excess kurtosis $\mathcal{K}_e$ with the observed $\mathbb{E}_\parallel$; (iii) quantitatively document the positive correlation of model-independent observations of the runaway density fraction δ with solar wind speed; (iv) quantitatively demonstrate with observations the strong correlation of $\delta(\mathbb{E}_\parallel)$ predicted by Dreicer's theoretical work (1959, 1960); (v) quantitatively document SERM's recovery of $\delta \propto \tau^{-2}$ seen in the data; (vi) use the predicted radial gradient of the SERM eVDF properties across a published two-fluid solution with the Spitzer closure to contradict the closure's assumed Maxwellian eVDF; and (vii) show SERM's predicted strong evolution of excess kurtosis with increasing radial distance from the Sun.

2. Dreicer's Insight

The seminal insight of Dreicer (1959, 1960) was his theoretical demonstration of the peculiar response of a fully ionized plasma to its immersion in a finite $E_\parallel$. In the presence of such an electric field Dreicer (1960) deduced the occurrence of a bifurcation of the topology of the electron integral curves (trajectories) in velocity space about a saddke point, S_D, indicated in Figure 1 between the cyan and green integral curves. These curves have cylindrical symmetry out of the plane of Figure 1 that contains $E_\parallel$. The parameter involved in the two types of trajectories is an integration constant Dreicer called K. The integral curves of these two classes are based on the sign of K. The jumps in K are controlled by the diffusion in energy, which was not treated by Dreicer's initial works. Jumps across the separatrix by diffusion were not retained by Dreicer and would involve a change in the sign of K, allowing slow migration from overdamped to underdamped populations.

With this finding the speed dependence of Coulomb collisions and finite $E_\parallel$ locally induce a lowest-order compartmentalization in velocity space properties and thus for eVDF. This identification differentiates the electrons in the two compartments as having intrinsically different antecedents and thus properties: one is essentially localized by Coulomb collisions that favorably damp out the accelerating ability of $E_\parallel$; the other compartment's electrons gain more energy from
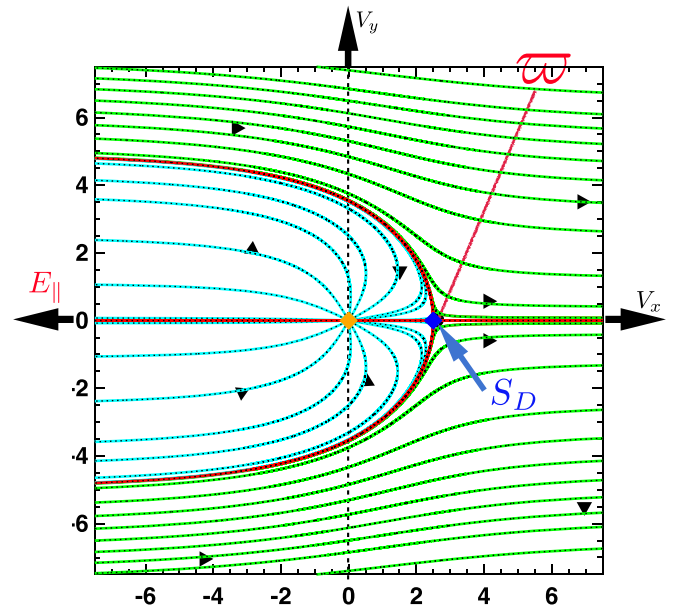
Figure 1. Dreicer's (1960) electron integral curves (electron trajectories) moving in $E_\parallel$ with ion drag. All velocities are in thermal speed units. Red horizontal line ($v_\perp = 0$) and curved red parabola give two separatrices that cross at the blue saddle point S_D, located at $v_\parallel = \varpi$. Pairs of cyan and green integral curves on either side of the parabola bifurcate about the saddle point, diverging in opposite directions from the red parabolic separatrix. Cyan integral curves converge on the orange node at $|v| = 0$. Green integral curves proceed from $v_x = -\infty$ at finite $v_{o,y}$ to $v_x = \infty$ at generally lower $v_y < v_{0,\perp}$. The integral curves shown are the intersection of cylindrically symmetric integral curves with a plane containing the electric field direction. This projection effect produces the mirror symmetry of the traces.

$E_\parallel$ than they lose by ion drag. Thus the electrons in the latter zone are promoted in energy, while the former component's electrons are only weakly modified in kinetic energy by their interaction with $E_\parallel$. These two zones are analogous to the *local* and *global* electron classes identified previously by Scudder & Olbert (1979a).

SERM's thesis is that Dreicer's bifurcation is the cause of the nonthermal eVDF. In addition, this viewpoint suggests the fraction of electrons that should be found in the global population of the suprathermals, a relation unforeseen by Scudder & Olbert (1979a, 1979b) that is now subject to experimental test. With the advent of local determinations of $E_\parallel$ it is possible to test this hypothesis by asking the proper questions of the measured eVDF, which this paper will discuss.

Dreicer's insight would appear to be important for all astrophysical plasmas since collisions and $E_\parallel$ are virtually assured to be present; further, sizable dimensionless $\mathbb{E}_\parallel = \mathcal{O}(1)$ is almost a certainty between the stars.

However, the profiles of these ingredients in fluid solar wind models are often deemphasized by adopting a single fluid momentum equation, bulk collision rates, ignoring the thermal force, and adopting questionable truncation closures. Although $E_\parallel(\mathbf{r}) \neq 0$ occurs in published fluid solutions, its size is only determined by post-processing the fluid solution to unpack $E_\parallel$ from a possibly incomplete electron or ion momentum equation.

Although exospheric treatments ignore collisions, they solve for $E_\parallel(s)$ as the important unknown and consider other deterministic forces like gravity and centripetal accelerations. Competitive decelerations by collisions were not considered until recently, when they were introduced by assuming

nonthermal boundary conditions (Scudder 1992b, 1992c; Maksimovic et al. 1997; Zouganelis et al. 2004). A property of the treatment of the wind problem as a Vlasov problem is that the assumed eVDF boundary conditions *can stream* along accessible orbits to the interior of the solution without being produced there.

Dreicer's modeling includes the more realistic consideration where (i) Coulomb collisional drag resists $E_\parallel$, while also pointing out (ii) that the speed dependence of Coulomb collisions always allows some of the electrons to be more nearly collisionless. This model also suggests there is a finite promotion in the energy of electrons across the red separatrix in Figure 1, transforming initially overdamped collisional electrons into locally energizing underdamped ones. In astrophysical plasmas this competition is more important as r increases, since the other forces, like gravity or neutral drags, weaken rapidly with increasing stellar radius. The winds that form around stars extend the *plasma* density to much larger radii than where neutral gases are usually found. Being plasmas these astrophysical competitions are essentially those Dreicer modeled, except the origin of $E_\parallel$ is internal rather than externally applied in his motivating laboratory plasma and invariably is attended by pressure gradients.

Dreicer's dimensionless electric field $\mathbb{E}_\parallel$ (Equation (1)) *scales* the size of electron acceleration caused by $E_\parallel$ by the size of the Coulomb collisional deceleration experience by a fiducial thermal-speed electron's scattering off of all ions. His laboratory model problem did not consider forces beyond the electric and Coulomb forces.

In Dreicer's model two topologically different classes of electron trajectories (integral curves) were identified. These color-coded curves in Figure 1 reveal Dreicer's discovery: *velocity space bifurcation of integral curves* about the saddle point at S_D, where $v_x = \varpi$.

This bifurcation is seen by the change in the topology of the differently colored integral curves of the two different types approaching S_D. Moving parallel to, but on opposite sides of, the (red) parabola these curves make strikingly different course adjustments around the saddle point: the cyan trajectories turn toward lower speeds, heading to the origin, while the green trajectories turn to increase their speeds with increasing distance from the red parabolic separatrix. These two different topologies of integral curves reflect the bifurcation that creates two distinguishable groups of electrons with different typical properties.

For the cyan integral curves in Figure 1 the magnitude of the speed-dependent ion Coulomb drag overpowers the magnitude of the electric acceleration; electrons on these curves are referred to as *overdamped* (Scudder 2019c). Along the green integral curves, the magnitude of the electric acceleration overpowers the magnitude of the decreasing speed-dependent friction, leading to an increasing net electron acceleration with increasing speed. Dreicer (1959, 1960) called this *underdamped* secular process *electron runaway*.

The velocity space stream lines are topologically different in these distinct volumes separated by the red parabolic separatrix in Figure 1. The overdamped stream lines have a bounded extent along the direction of the electric force, ultimately converging at zero speed (orange dot at the ion rest frame). The underdamped electrons' phase-space trajectories are unbounded, connecting negative V_x and positive V_x at large

speeds. The overdamped stream lines are further impacted at lower speeds by diffusive energy exchange with other electrons as their integral curves converge on the origin of velocity space; these low-speed effects and the weak diffusion across the red parabola were neglected by Dreicer in deriving these integral curves.

Dreicer's runaway insight was used to explain early disruptions of laboratory fusion experiments, where large applied $E_\parallel$ led to a super-electron thermal-speed hydrodynamic drift separation of nearly all electrons from the background ions. When this drift occurred, it was called *bulk runaway* and was accompanied by strong parallel dimensionless electric fields in the sense defined by Dreicer (see Equation (1)). Such bulk runaway generated a sizable $J_\parallel$, whose divergence disrupted quasi-neutrality, and led to loss of confinement and a short circuiting of the desired steady-state energization in the limited laboratory experiment.

In Appendix B a modern variant of Dreicer's analysis by Fuchs et al. (1986) is shown to produce an analogous bifurcation of velocity space and supports Dreicer's sufficient conditions for occurrence of underdamped runaways. In Figure 17 the separatrices determined by Dreicer and Fuchs et al. (1986) are illustrated for the same parameters. This analysis also suggests the underdamped region is no longer open ended as in Dreicer's less complete treatment. Important quantitative distinctions between the two treatments and boundary locations occurring primarily for high-Z laboratory plasma runaway are discussed there and in Scudder (2022a).

2.1. Dimensionless $E_\parallel$ is Key: $\mathbb{E}_\parallel$

Dreicer organized his predictions in terms of his dimensionless parallel electric field $\mathbb{E}_\parallel$:

$$\begin{aligned} \mathbb{E}_\parallel &\equiv \frac{|eE_\parallel|\lambda_{\mathrm{mfp}}}{2k_B T_e} \\ &\equiv \frac{|eE_\parallel|}{|e|E_D} \\ &\neq |E_\parallel|, \end{aligned} \tag{1}$$

where λ_{mfp} is the Coulomb mean free path for the thermal-speed electron Coulomb scattering off of all ions. This dimensionless quantity gauges the relative size of the electric force on any electron to the sum over all ion collisional drag forces, $|e|E_D = 2k_B T_e/(\lambda_{\mathrm{mfp}})$, felt by a fiducial thermal-speed electron (see Appendix C). Equation (1) shows that Dreicer's *dimensionless* parallel electric field, $\mathbb{E}_\parallel$, is neither a vector nor the magnitude of the parallel electric field.

2.2. Minimum Runaway Speed ϖ

The minimum runaway speed in thermal speed units, ϖ, occurs at the apex of the parabolic red separatrix that is also the site of the saddle point of the bifurcation in Figure 1. Its speed is completely determined by $\mathbb{E}_\parallel$,

$$\varpi^2 \equiv \frac{3}{\mathbb{E}_\parallel}, \tag{2}$$

and is located along the direction of the electric force on an electron.

2.3. eVDF Response to $\mathbb{E}_\parallel$ Changes

(i) As $\mathbb{E}_\parallel$ increases the minimum runaway speed ϖ *decreases* and the fraction of the electron density on the green runaway integral curves *increases*.

(ii) In thermodynamic equilibrium $\mathbb{E}_\parallel = 0$ and $\varpi \uparrow \infty$ and there are *no* runaways nor suprathermals.

(iii) When collisions are very frequent $\mathbb{E}_\parallel \downarrow 0$ and the underdamped regime, $v_\parallel > \varpi$, recedes toward infinity and a Maxwellian can consistently be expected to dominate the eVDF in the overdamped electrons.

(iv) The idealization of collisionless plasma with finite $E_\parallel$ allows only the underdamped class. As is well known, the eVDF in this Vlasov circumstance is determined from the assumed boundary conditions for the eVDF and is a collisionless sheath problem.

(v) At any finite collision frequency $\mathbb{E}_\parallel$ is finite and the eVDF will be bifurcated above $v_x > \varpi$ and observably nonthermal.

For the common situation where $E_\parallel \neq 0$ *some* electrons are always able to runaway, even when bulk runaway is not possible. This omnipresent runaway supplies the electron heat conduction skew to the eVDF, while simultaneously challenging the plasma to remain free of parallel currents. The steady-state resolution of this potential for current flow is discussed in a sequel paper about odd moments and heat flow (J. D. Scudder 2023, in preparation).

2.4. SERM Suitability for Solar Wind

The SERM model is suitable for describing the solar wind since the observed charge number fluxes of electrons and ions are observationally well matched (see Salem et al. 2021, see their Figure 13), implying the electron solar wind moments in the ion rest frame suggest no large $J_\parallel$.

In Dreicer's consideration his $E_\parallel$ represented the only force parallel to the magnetic field competing with collisions. The electron momentum equation for the solar wind, including pressure, inertial and thermal force effects, implies that the net acceleration on the overdamped population that could drive bulk runaway is considerably ($<80\%$) smaller than $\mathbb{E}_\parallel$. A 4 yr survey of $\mathbb{E}_\parallel$, shown in Figure 7 (Scudder 2022a), shows that this effective electric field $\mathbb{E}_\parallel(\mathrm{sw})$ is typically insufficient to drive the solar wind into bulk runaway. This estimate is consistent with the routinely reported well-matched charge number flux of electrons and ions.

2.5. Runaway Density Fraction, δ

Dreicer suggested that the runaway density fraction, δ, caused by all electrons on the green integral curves of the eVDF would be a strong increasing function of $\mathbb{E}_\parallel$. This expectation is tested empirically with solar wind observations below in Figure 5.

2.6. Runaways Suprathermals Are Harder than Thermals

The runaways were suggested to possess a harder energy spectrum than the softer spectrum for the underdamped energy range. A 4 yr correlation of Wind halo spectral indices has shown the hardness of those spectra is positively correlated with the size of $\mathbb{E}_\parallel$, as would be expected from that population being seeded by runaway energization (see Figure 22 of Scudder 2022a).

2.7. Summary of Dreicer Bifurcation

By incorporating Dreicer's seminal discovery, SERM has suggested a required astrophysical scenario for explaining the ubiquitous occurrence of nonthermal eVDFs. Validating SERM's predictions with a 4 yr data set using solar wind eVDF measurements would provide a strong in situ astrophysical foundation for this suggestion. To be sure, this is not a complete resolution of how the astrophysical system accommodates such disruptions to local thermodynamic equilibrium in forming interstellar winds. In particular, the competing pressure gradient profiles of these plasmas are not yet obviously set by these considerations; the determination of the pressure profiles that mesh with SERM's suggestion require consideration of the transport equations for the system, not simply testing local mechanism characteristics as provided by SERM alone.

Early one-fluid models of the the solar wind artfully avoided the explicit consideration of the role of collisions and $E_\parallel$. Two-fluid solutions struggled with the size of $E_\parallel$ and suitable closures. The exospheric calculations modeled the wind as a collisionless sheath producing improved-fidelity $E_\parallel$ but ignored collisional effects altogether. The first suggestions of the cause of the nonthermal eVDFs in the wind involved considerations that attempted joint descriptions of the speed dependence of the Rutherford cross section and $E_\parallel$ (Scudder & Olbert 1979a; Olbert 1983; Scudder 1996; Landi & Pantellini 2001; Scudder 2019c).

3. Excess Kurtosis

Before detailing the eVDF properties predicted by SERM and Dreicer, it is important to emphasize the expected production by $\mathbb{E}_\parallel$ of positive excess kurtosis, $\mathcal{K}_e$. Excess kurtosis is the first place in the fluid moment hierarchy where the non-Gaussian character of the eVDF may be quantitatively measured in a model-independent way.

Specifically, the excess kurtosis for electrons, $\mathcal{K}_e$, is defined in the fluid's comoving frame as the ratio of the fourth moment *per particle* to the square of the second moment *per particle* less a constant

$$\mathcal{K}_e = \frac{\langle |\boldsymbol{v} - \boldsymbol{U}|^4 \rangle}{\langle |\boldsymbol{v} - \boldsymbol{U}|^2 \rangle^2} - \frac{5}{3}, \tag{3}$$

chosen so that $\mathcal{K}_e$ is identically zero for a Maxwellian eVDF. $\mathcal{K}_e$ is positive for a *leptokurtic* eVDF and negative for a *platykurtic* eVDF. At a given location $\mathcal{K}_e$ can be determined from the model-independent eVDF alone without *any* knowledge of the size of $\mathbb{E}_\parallel$.

A two-dimensional (2D) histogram of the 4 yr column-normalized probability of observed Wind 3DP pairs $[\mathcal{K}_e(t), \mathbb{E}_\parallel(t)]$ is shown in Figure 2. The set of blue dots within the bright yellow region of the highest probability (in each column) suggests the variation of the most likely $\mathcal{K}_e(\mathrm{BBE})$ encountered with $\mathbb{E}_\parallel$. SERM's expected positive correlation is recovered from input data values each spanning more than an order of magnitude.

The observed excess electron kurtosis ranges between $0.1 < \mathcal{K}_e < 10$; it has a 4 yr mode of $\mathcal{K}_e \simeq 1.8$, exceeding the usual noteworthy dimensionless statistical measure (unity) for overpopulated suprathermal tails.

The observed positive correlation of $\mathcal{K}_e > 0$ and $\mathbb{E}_\parallel$ presented in Figure 2 during 4 yr of Wind observations is
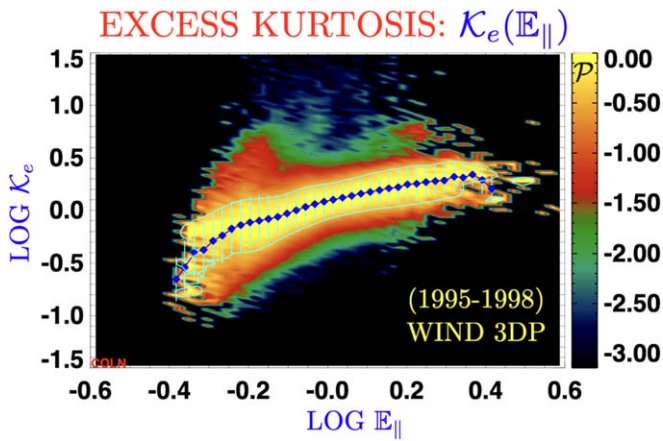
Figure 2. Excess electron kurtosis $\log \mathcal{K}_e$ vs. $\log \mathbb{E}_\parallel$. A Maxwellian eVDF has $\mathcal{K}_e \equiv 0$. The ordinate is determined solely from 3DP moments; the abscissa is determined solely from prior ambipolar electric field analysis using a cut of the eVDF along the magnetic field line opposite to the heat flux as discussed in Scudder (2022a). Positive log–log correlation is clearly demonstrated.

consistent with SERM's thesis that Dreicer runaway production is the cause of the *ubiquitously nonthermal* eVDF seen in the solar wind since Montgomery et al. (1968). More detailed quantitative tests will be presented below to support this thesis.

Examples of rarely occurring small excess electron kurtosis $0 < \mathcal{K}_e \lesssim 0.1$ (and the most nearly Maxwellian eVDFs) do occur at 1 au. Consistently, these spectra are observed to accompany the rarest, weakest observed extremes of $\mathbb{E}_\parallel$. Because $\mathbb{E}_\parallel$ and solar wind speed are statistically correlated over 4 yr at 1 au (Scudder 2022a), more nearly Maxwellian eVDFs with smaller $\mathcal{K}_e$ are expected and seen in the more collisional slow wind (but not shown), where the mean free path for Coulomb collisions is systematically smaller than in higher wind speeds.

4. Observations: $\mathcal{T}_h/T_c$ versus $\mathbb{E}_\parallel$

A frequently reported measure of the nonthermal state of solar wind electrons is the shallower logarithmic slope of the eVDF at suprathermal compared to thermal energies. This morphology implies that the logarithmic derivative temperature, $\mathcal{T}_h$, at suprathermal energies is larger than the same measure, T_c, in the lowest core-dominating energy range. Since these measures of temperature are related to derivatives in disjoint intervals of energy, they can reflect more directly the difference between the eVDF shape in the suprathermal and thermal domains.

As routinely reported at 1 au, the ratio of these two pseudo-temperatures is slowly varying on several hour timescales in the data, with typical median values of 5–6 and generally ranging between 4 and 10 at 1 au. This morphology, known since 1968, remained unexplained until the SERM model's calculation that reproduced it (Scudder 2019c) and predicted its relationships with the density fraction of runaways, δ.

The omnipresence of the spectral break implied by $\mathcal{T}_h \neq T_c$ effectively precluded characterizing the electrons as a single, near-Maxwellian phase space. Since the observed ratio always exceeds unity the adjective *leptokurtic* is more precise than *nonthermal* for the routinely observed solar wind eVDF. The initial explanation for its occurrence was made using a simplified kinetic equation incorporating the speed dependence
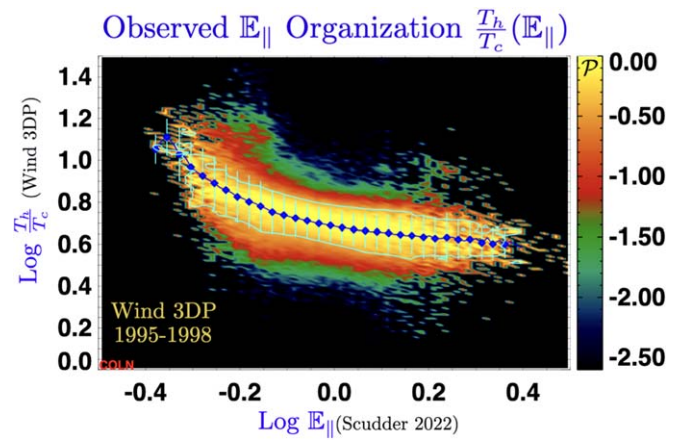
Figure 3. 1 au column-normalized probability of occurrence of Wind 3DP observed $\mathcal{T}_h/T_c$ vs. observed $\mathbb{E}_\parallel$ synthesized from over 279,000 data points measured at the forward Lagrange point during the interval 1995–1998.

of the Coulomb scattering cross section (Scudder & Olbert 1979a, 1979b).

The SERM model had predicted (Scudder 2019c) that the ratio

$$\tau \equiv \frac{\mathcal{T}_h}{T_c} = g(\mathbb{E}_\parallel) \tag{4}$$

should be a 1:1 function of $\mathbb{E}_\parallel$. When the initial SERM predictions were made (Scudder 2019c) there were no in situ $\mathbb{E}_\parallel$ observations to test SERM's prediction. Using the WIND 3DP data set and the newly available determinations of $\mathbb{E}_\parallel$ at the Wind 3DP cadence (Scudder 2022a), it is now possible to sustain SERM's prediction.

Figure 3 shows the first observations of a strong organization of $\mathcal{T}_h/T_c$ by $\mathbb{E}_\parallel$; by their pattern the blue centroids are compatible with reflecting a 1:1 relationship between the most probable values of $\mathcal{T}_h/T_c(\mathbb{E}_\parallel)$ and $\mathbb{E}_\parallel$.

At first this anticorrelation may seem unreasonable until it is realized that smaller $\mathbb{E}_\parallel$ implies larger minimum runaway kinetic energy, $\mathcal{E}_\varpi$, and thus smaller allowed runaway density fractions, requiring higher effective temperature ratios, as seen in Figure 3.

5. Observations: $\mathcal{T}_h/T_c$ versus n_h/n_c

A 50 yr old observed anticorrelation between $\mathcal{T}_h/T_c$ and n_h/n_c was also explained by SERM (Scudder 2019c). In terms of the SERM shape parameters, the ratio of slope temperatures is essentially τ^{-2}:
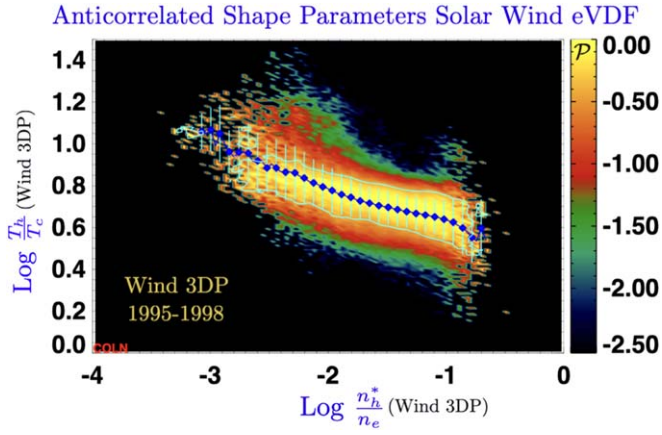
$$\mathcal{T}_h/T_c \simeq \tau^{-2}. \tag{5}$$

Estimates for 1 au parameters in an Appendix of Scudder (2019c) showed that

$$\delta^{3DP} \simeq \delta^* \simeq n^*_h/n_e \simeq 0.59 n_h/n_e \tag{6}$$

would be close to the theoretically expected runaway fraction, δ. Figure 4 illustrates the observed correlation with Wind 3DP data using 4 yr of data of $\mathcal{T}_h/T_c$ with n^*_h/n_e, showing their inverse correlation:

$$\mathcal{T}_h/T_c^{\text{obs}} \propto 1/\delta^*. \tag{7}$$

The full 4 yr data set illustrates the clear anticorrelation between the approximate runaway fraction $\delta \simeq 0.59 n^*_h/n_e$

Figure 4. Probability of occurrence of observed T_h/T_c vs. n_h^*/n_e over 4 yr data set acquired between (1995–1998) at 1 au forward Lagrange point.

and $T_h/T_c \simeq \tau^{-2}$:

$$\delta^{\mathrm{obs}} \propto \tau^{\mathrm{obs}-2}. \tag{8}$$

These correlations among the Wind observables in Equations (8) and (7) suggests if $\mathbb{E}_\parallel$ were an observable that δ and $\mathbb{E}_\parallel$ would be positively correlated:

$$\delta \propto \mathbb{E}_\parallel. \tag{9}$$

This suggestion was made in SERM (Scudder 2019c) as foreshadowing the signature of Dreicer's bifurcation insight in the available archival data presented.

Before documenting Equation (9) with model-independent simultaneous measurements of δ and $\mathbb{E}_\parallel$ in Figure 5 below, a brief review is presented of Dreicer's insight.

6. Dreicer Runaway Density Fraction, δ

Dreicer estimated the density fraction, δ^{Max}, presuming a Maxwellian eVDF plasma was placed in a nonzero electric field. He found $\delta(\mathbb{E}_\parallel)$ to be a *strongly increasing function of increasing* $\mathbb{E}_\parallel$ (Dreicer 1960, Equation (8)).

Dreicer defined δ by computing the density fraction outside the *red parabolic* separatrix in Figure 1. The parabola's location is parametric in the size of $\mathbb{E}_\parallel$; its shape is determined by the specific speed dependence of Coulomb friction (see Equation (10)). The cylindrically symmetric separatrix boundary is implied by the joint conditions:

$$|\boldsymbol{w}|^2 = v_\varpi^2 \sec^2 \frac{\theta}{2}$$

$$\cos \theta \equiv \frac{-\boldsymbol{w} \cdot E_\parallel \hat{\boldsymbol{b}}}{|\boldsymbol{w}||E_\parallel|}$$

$$\boldsymbol{w} \equiv |\boldsymbol{v} - \boldsymbol{U}|, \tag{10}$$

where θ maps out a polar angle from the direction of $E_\parallel \hat{\boldsymbol{b}}$ and $\boldsymbol{U}$ is the velocity of the ion center of mass (Dreicer 1959, 1960).

This separatrix leads to Dreicer's integral for the runaway density fraction from an assumed gyrotropic eVDF:

$$\delta = \frac{2\pi \int_0^\pi d\theta \sin \theta \int_{v_\varpi \sec \theta/2}^\infty dw w^2 f_e(\boldsymbol{w})}{\int_{\mathrm{all}} d^3 \boldsymbol{w} f_e(\boldsymbol{w})}. \tag{11}$$
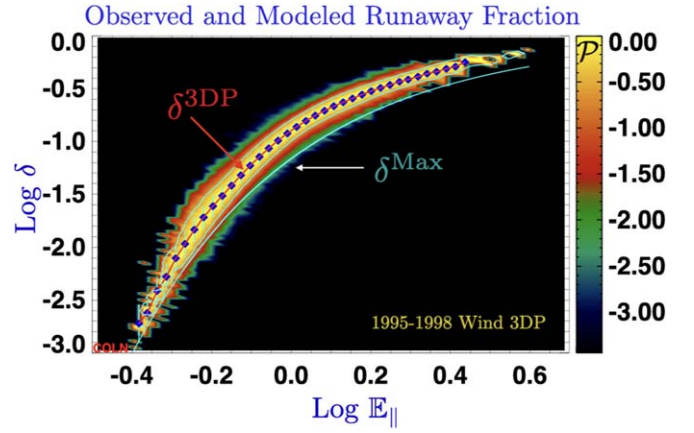
Figure 5. Cyan: variation of Dreicer's runaway fraction δ^{Max} with $\mathbb{E}_\parallel$ presuming a Maxwellian eVDF. Colored contour: probability of detection over 4 yr of the measured runaway fraction, δ^{3DP}, vs. the self-consistent measurement of $\mathbb{E}_\parallel$ (Scudder 2022a). Blue diamonds are the column average positions of the observed probability of occurrence. The pattern of Wind 3DP blue diamonds closely follows a trend with $\mathbb{E}_\parallel$ of Dreicer's estimate in cyan, but are invariably slightly above Dreicer's estimate while tracking one another over three orders of magnitude. See Figure 6 for further details.

Assuming a Maxwellian eVDF for f_e, this integral becomes

$$\delta^{\mathrm{Max}}(\varpi) = \frac{2\varpi}{\sqrt{\pi}} \exp(-\varpi^2) + (1 - 2\varpi^2)\mathrm{erfc}(\varpi). \tag{12}$$

Dreicer's reported estimate for Equation (12) retained only the initial product term, assuming $2/\sqrt{\pi} \simeq 1$, revealing an exponential sensitivity on $\varpi^2 = 3/\mathbb{E}_\parallel$. In this way he suggested that the runaway density fraction grows strongly with increasing $\mathbb{E}_\parallel$. The full prediction of Equation (12) is shown by the cyan curve labeled δ^{Max} in Figure 5.

Dreicer's asymptotic approximation was only valid for large $\varpi >> 1$ (very small $\mathbb{E}_\parallel$) that is *inadequate* for our wider range of $\mathbb{E}_\parallel$. Maxwellian eVDFs in a plasma with collisions are only naturally self-consistent when $E_\parallel = 0$, an uninteresting assumption for estimating the fraction of runaways in astrophysics. The determination of δ using an observed eVDF will change the details of the predicted runaway density fraction but not its overall strong dependence on $\mathbb{E}_\parallel$.

Dreicer's unapproximated single-Maxwellian-based estimate for $\delta(\mathbb{E}_\parallel)$ is denoted as δ^{Max} when using Equation (12). The runaway density fraction determined from the Wind 3DP measurements are denoted as δ^{3DP}. For the same range of $\mathbb{E}_\parallel$ the variation of δ^{3DP} from the observed eVDF has a comparable dynamic range as found with Dreicer's suggestion, δ^{Max}, using the complete integral shown in Equation (12).

6.1. Observed Runaway Density Fraction $\delta^{\mathrm{3DP}}(\mathbb{E}_\parallel)$

The probability of occurrence over 4 yr in the 2D space of the simultaneously observed pairs of $[\mathbb{E}_\parallel(t), \delta^{\mathrm{3DP}}(t)]$ is shown in the log–log 2D color-coded, column-normalized histogram of Figure 5. A thin, concentrated locus of column-normalized probability for the observed data pairs $[\mathbb{E}_\parallel, \delta^{\mathrm{3DP}}]$ drops three orders of magnitude from bright yellow to black background (moving transverse to the arc), implying a well-defined channel in the independent variables. Its yellow *crown* is the locus of all points above a column-normalized occurrence probability of e^{-1}.
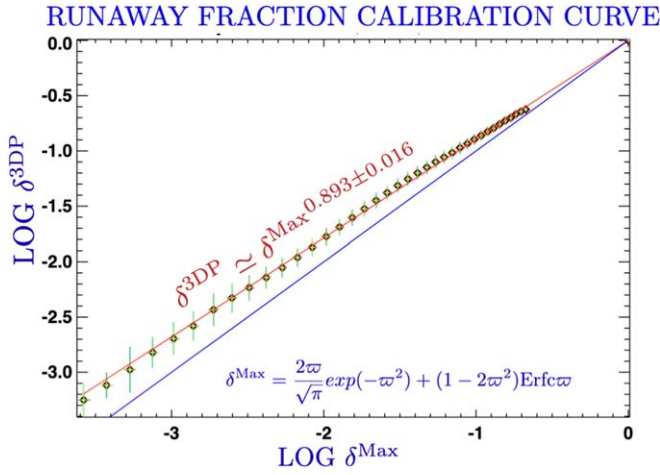
Figure 6. Ordered pairs from Figure 5 for $[\delta^{\mathrm{Max}}(\mathbb{E}_\parallel), \delta^{\mathrm{3DP}}(\mathbb{E}_\parallel)]$ (diamonds) together with best-fit linear regression in red with slope of the form $\delta*\,3\mathrm{DP} = \delta^{\mathrm{Max}}(\varpi^2)^{0.893}$. For comparison the solid blue curve has a unit slope.

This extent of the ordinate values implied by the yellow arc extends over three orders of magnitude of runaway density fraction, δ. The blue diamonds and horizontal error flags are determined from $\langle\mathbb{E}_{\parallel_o}\rangle$ within a x-axis column of the histogram and have ordinates and vertical error flags set by the mean value of $\langle\delta^{\mathrm{3DP}}(\mathbb{E}_{\parallel_o})\rangle$ weighted by the column entries' normalized probabilities of detection. A red curve connecting the blue diamonds indicates the cross-column trend of blue column means as $\mathbb{E}_\parallel$ varies. The cyan flags at the blue diamonds denote the variance in the ordinate, again weighted by normalized probability.

The continuous superposed smooth narrow cyan curve illustrates Dreicer's $\delta^{\mathrm{Max}}(\mathbb{E}_\parallel)$ using Equation (12). Over three orders of magnitude the trend of $\delta^{\mathrm{3DP}}(\mathbb{E}_\parallel)$ resembles Dreicer's cyan curve, $\delta^{\mathrm{Max}}(\mathbb{E}_\parallel)$. Virtually *all* perceptible observed 3DP probabilities (colored regions) from 4 yr of data are totally *above* Dreicer's cyan curve. Certainly the average locus of blue diamonds connected by the red curve for δ^{3DP} is above the predicted value from Dreicer's cyan curve $\delta^{\mathrm{Max}}(\mathbb{E}_\parallel)$.

### 6.2. Calibrating Runaway Fraction versus $\mathbb{E}_\parallel$

The coordinated variation of $\delta^{\mathrm{3DP}}(\mathbb{E}_\parallel)$ versus $\delta^{\mathrm{Max}}(\mathbb{E}_\parallel)$ seen in Figure 5 is significantly simplified by the red diamonds plotted on log–log paper in Figure 6 after suppressing their functional dependences on $\mathbb{E}_\parallel$. The vertical error flags for $\delta^{\mathrm{3DP}}(\mathbb{E}_{\parallel_o})$ in Figure 6 have been transferred from those for the blue diamonds in Figure 5, and the abscissa and its errors are implied by the bin average of $\mathbb{E}_{\parallel_o}$ and uncertainty as they propagate through Equation (12) for the indicated value and uncertainty for $\delta^{\mathrm{Max}}(\mathbb{E}_{\parallel_o})$ needed for this log–log format.

Synthesizing over 279,000 separate observations over 4 yr in the solar wind, the 38 bin-averaged points in this picture are unexpectedly well fit by a simple power-law *calibration curve* of the form

$$\mathrm{Log}\,\delta^{\mathrm{3DP}} = (0.893 \pm 0.016)\mathrm{Log}\,\delta^{\mathrm{Max}}$$
$$\delta^{\mathrm{3DP}} \simeq (\delta^{\mathrm{Max}})^{0.893\pm0.016}. \tag{13}$$

Since $\delta^{\mathrm{Max}} < 1$, the exponent in Equation (13) being less than unity reflects the observed 3DP runaway fraction at $\mathbb{E}_\parallel$ always
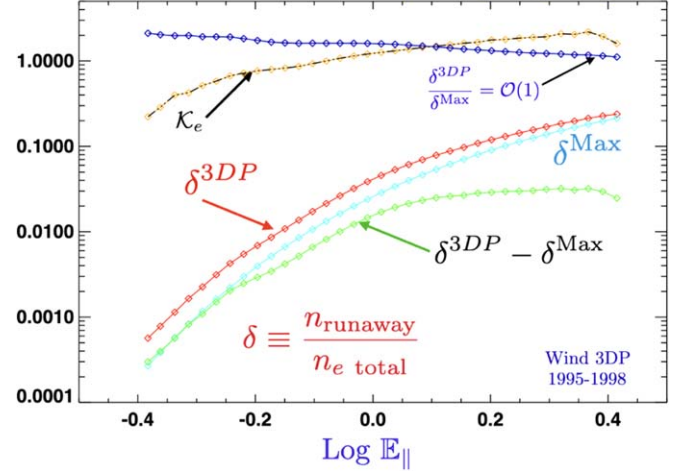
Figure 7. Variations of observed δ^{3D} and δ^{Max} with dimensionless parallel electric field $\mathbb{E}_\parallel$. Noteworthy is the decrease in excess kurtosis, signifying a more Maxwellian-like eVDF accompanying the decreasing difference of $\delta^{\mathrm{3D}}{-}\delta^{\mathrm{Max}}$.

exceeding that of a Gaussian using $\delta^{\mathrm{Max}}(\mathbb{E}_\parallel)$ for the same value of $\mathbb{E}_\parallel$, as shown by the red and cyan curves in Figure 7.

This calibration curve can be transformed into a predictive formula for $\delta^{\mathrm{3DP}}(\varpi(\mathbb{E}_\parallel))$, indicated by the asterisk:

$$\delta*(\varpi) = \left(\frac{2\varpi}{\sqrt{\pi}}\exp(-\varpi^2) + (1 - 2\varpi^2)\mathrm{erfc}\,\varpi\right)^{0.893\pm0.016}. \tag{14}$$

Arguably the trend of diamonds from δ^{3DP} is a more accurate predictor of the observations than Dreicer's estimate. With care this calibration can explore the implications of Equation (14) over a wider range of $\mathbb{E}_\parallel$ than available in the Wind 3DP data used to ascertain the calibration curve.

The observed and Dreicer's predicted runaway fractions are $\mathcal{O}(1)$ with respect to one another, even while their δ magnitudes track over three orders of magnitude:

$$\frac{\delta^{\mathrm{3DP}}}{\delta^{\mathrm{Max}}} = (\delta^{\mathrm{Max}})^{-0.11} = \mathcal{O}(1). \tag{15}$$

Tabulating this shallow exponent's prediction over the observed range of δ in Figure 7 establishes the $\mathcal{O}(1)$ estimate. This and other relationships are shown in Figure 7. The nonnegative difference $\delta* - \delta^{\mathrm{Max}}$ generally decreases with decreasing δ^{Max}, especially when $\delta^{\mathrm{Max}} < 0.35$. Excess kurtosis, $\mathcal{K}_e$, was previously shown to decline with decreasing $\mathbb{E}_\parallel$ (Figure 2), the regime where the eVDF becomes increasingly more Maxwellian. Thus, the model-independent determinations of $\mathcal{K}_e$ predict, as seen in this trend, the convergence in weak $\mathbb{E}_\parallel$ regimes of $\delta^{\mathrm{3DP}}(\mathbb{E}_{\parallel_o}) \downarrow \delta^{\mathrm{Max}}(\mathbb{E}_{\parallel_o})$.

These interrelationships and trends are compared in Figure 7, showing the log–log trends with $\mathbb{E}_\parallel$ of (i) kurtosis $\mathcal{K}_e$ (orange), (ii) δ^{3DP} (red), (iii) δ^{Max} (cyan), (iv) the difference $\delta^{\mathrm{3DP}} - \delta^{\mathrm{Max}}$ (green), and (v) $\delta^{\mathrm{3DP}}/\delta^{\mathrm{Max}}$ (blue). These trends are digests of the average trends of probability extracted from blue diamonds in Figures 2 and 5.

This raises some salient points. (i) Across the entire observed range of $\mathbb{E}_\parallel$ that $\delta^{\mathrm{3DP}} = \mathcal{O}(1)\delta^{\mathrm{Max}}$ (blue dashed), thus Dreicer's
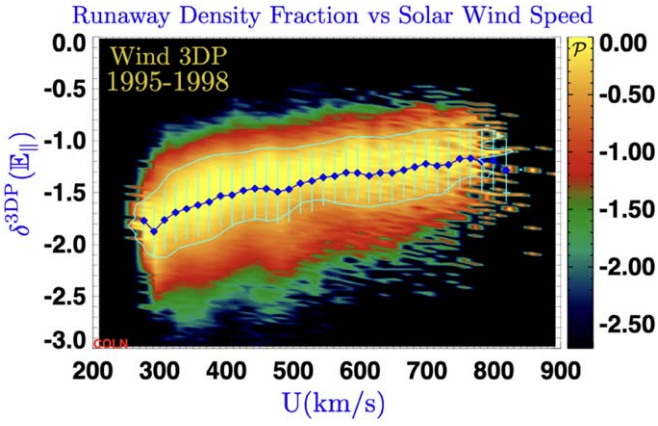
Figure 8. Wind 3DP determination of the normalized probability of the occurrence of the Dreicer runaway density fraction, δ^{3DP}, as a function of solar wind speed, U. Data acquired in 1995–1995 on the Wind spacecraft at the forward Lagrangian point. The ridge of the highest probability of occurrence is indicated by the bright yellow coloring.

estimate of δ^{Max} *is* the correct order of magnitude as $\mathbb{E}_{\parallel}$ varies, as shown in the red and blue curves on this figure. (ii) All other quantities are monotonically increasing with the ambipolar electric field, $\mathbb{E}_{\parallel}$. (iii) The dynamic range of the δ quantities span three orders of magnitude. (iv) The green curve illustrates the convergence between the Wind-observed runaway fraction (red) and Dreicer (cyan) estimate as the observed $\mathbb{E}_{\parallel}$ decreases. (v) The solar wind eVDF is less kurtotic with more nearly Maxwellian properties when the Dreicer's δ^{Max} (cyan) curve approaches the red observations of δ^{3DP} as $\mathbb{E}_{\parallel}$ decreases. (vi) The sweeping decrease (green) in the difference $\delta^{3DP} - \delta^{Max}$ tracks the independently determined decreasing kurtosis (orange). By documenting these properties the observed convergence of the $\delta^{3DP} \rightarrow \delta^{Max}$ at low $\mathbb{E}_{\parallel}$ may be understood as observing circumstances more nearly consistent with those made in Dreicer's Maxwellian estimate in Equation (12).

6.3. Consistent Runaway $\delta^{3DP}(U)$

The probability of the occurrence of δ with solar wind speed, U, had been inferred from a diverse literature that spanned 40 yr of graphs in papers culled for the original discussion of SERM (Scudder 2019c); they provided anecdotal support for the SERM thesis. Figure 8 shows Wind 3DP measurements of internally consistent, time-synchronized runaway fraction δ^{3DP} using the measured $\mathbb{E}_{\parallel}$ as a function of measured wind speed; this histogram shows the 4 yr probability of the relationship only hinted at by the motivational Figure 1 in the discussion of Scudder (2019c).

Coming full circle, the previously shown correlation of $\mathbb{E}_{\parallel}$ with solar wind speed U (Scudder 2022a) reproduced here in Figure 9 can be viewed as the indirect corollary of the extremely tight correlation between δ^{3DP} and $\mathbb{E}_{\parallel}$ experimentally confirmed in Figure 5. Since above $\mathbb{E}_{\parallel}$ is observed to be positively, though less strongly, correlated with $|U|$, Figure 8 follows from Figure 5.

This is an interesting example of how the available solar wind speed may appear to be the relevant ordering parameter for δ, even though the more basic correlation explaining $\delta(U)$ is $\delta(U(\mathbb{E}_{\parallel}))$. Until the recent measurements of $\mathbb{E}_{\parallel}$ (Scudder 2022a) the Dreicer bifurcation remained only diffusely implied by attempts to inventory $\delta(U)$ (Scudder 2019c).
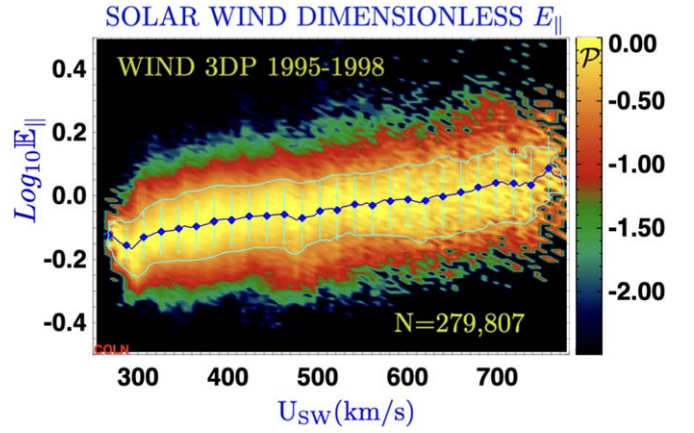
Figure 9. Previously reported positive correlation of measured $\mathbb{E}_{\parallel} = |E_{\parallel}|/E_D$ and solar wind speed (Scudder 2022a). Taken with Figure 8 this figure implies Dreicer's positive correlation between δ and $\mathbb{E}_{\parallel}$ exhibited in Figure 5.
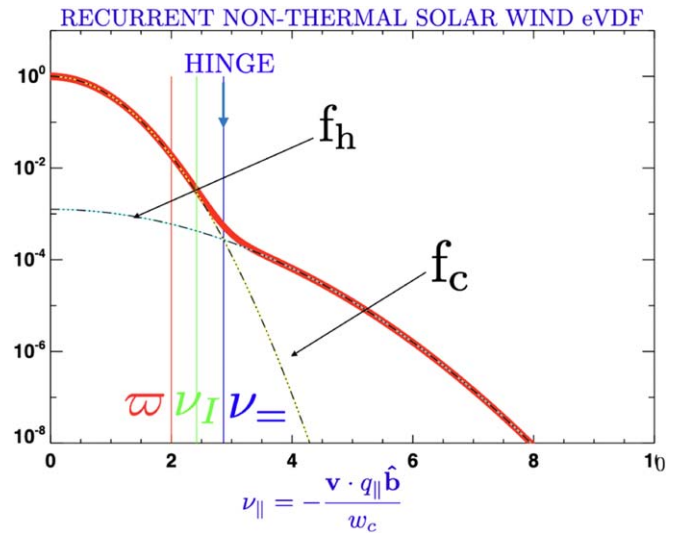
Figure 10. Significant locations on the solar wind eVDF (in red) cut along the magnetic field *opposite* from the heat-flux sense. Labels correspond to hinge $\nu_=$, inflection point ν_I, and minimum speed for runaway ϖ. Core and halo components have parabolic form with narrower and wider widths. The Wind 3DP intermediate characterization of the eVDF is performed by a superposition of core and halo components. The point where equal phase-space densities are added together is regarded as the *hinge*.

7. The Nonthermal Solar Wind eVDF

From their earliest characterizations electrons have been modeled as the superposition of two different functions of speed (initially Gaussians), as in Figure 10, in clear recognition of their bimodal parabolic trends on semi-log paper versus speed. The second component was mandated since when plotted versus energy the spectrum below 500 eV–1 keV clearly had at least two different slopes and thus energy scales.

Operationally, a *hinge* point is defined as where the two subcomponents used to fit the model-independent eVDF contribute equally to the eVDF. The speed of this hinge point in thermal speed units is denoted $\nu_=$, centered on the vertical blue line in Figure 10.

The influential survey by Feldman et al. (1975) tracked the variation with solar wind speed of the kinetic energy, E_B, of the eVDF break point determined as a pitch angle average about the heat-flow direction. A possible relation of this break energy with the exospheric potential energy barrier to infinity was also

explored, but a definitive conclusion was not drawn. This determination is clearly influenced by the skewness supporting the heat flux.

A cut through a typical eVDF at 1 au, shown in Figure 10, is indicated for electrons moving along the magnetic field *opposite* to the heat-flow direction. In this direction the modeling of the strahl is not involved. The *hinge point* at $\nu_=$ determines the associated dimensionless kinetic energy $\mathcal{E}_= = \nu_=^2$ identified in Scudder (2022a). Other labeled speeds correspond to the spectrum's inflection point ν_I and the minimum speed ϖ for runaway identified by Dreicer.

Electrons with speeds $\nu \geqslant \nu_\varpi$ are underdamped runaways; they correspond to contributors in the integrand of Equation (12) near $\theta = 0$. As is emphasized in this graph the inflection point and hinge point have speeds in excess of the minimum at ϖ required for runaway. The $\nu_=$ point on the eVDF has the opposite curvature of the negative curvature of eVDF at the runaway minimum speed ν_ϖ needed for measuring $E_\parallel$ (Scudder 2022a). Thus, geometrically $\nu_= \geqslant \nu_\varpi$.

In the first exploration of the SERM-I's premise its implications were explored assuming the building blocks of the eVDF were disjoint Gaussian components, assumed continuous at Dreicer's $\mathcal{E}_\varpi$; that model was constructed without independent knowledge of $\mathbb{E}_\parallel$ (Scudder 2019c) or of the hierarchical organization of the three important values of ν shown in Figure 10 identified when determining $\mathbb{E}_\parallel$ from the eVDF (Scudder 2022a).

For simplicity, SERM-I modeled a leptokurtic eVDF without a hinge, since it had assumed $\mathcal{E}_= = \mathcal{E}_\varpi$. Despite this model's predictive characteristics it was not known when producing specific regimes of δ and τ by this early version of SERM whether the specific values of $\mathbb{E}_\parallel$ supposed were quantitatively the correct, rather than approximate, local values involved!

With the intervening work $\mathbb{E}_\parallel$ has been determined for the Wind data set by identifying ϖ *based on the properties of the eVDF's curvature*. These new local measurements were quantitatively certified by comparing with independent pressure gradient information (see Figures 20 and 21 of Scudder 2022a). The detective work identifying $\mathbb{E}_\parallel$ also established that $\nu_= > \nu_\varpi$, as shown in Figure 10.

As a result, an improved version, SERM-II, is presented in this paper consistent with the corroborated $\mathbb{E}_\parallel$ that produces a more accurate leptokurtic model with a viable hinge point. This choice protects (i) consistency with externally corroborated, locally appropriate values of $\mathbb{E}_\parallel$; and (ii) produces better eVDF fidelity for inferring the ratio of partial pressures between thermal and suprathermal components.

8. Properties of the Electron Hinge

While preparing SERM-II a survey of the 4 yr Wind 3DP relationships between the lowest kinetic energy for runaway, $\mathcal{E}_\varpi$, and $\mathcal{E}_=$ was undertaken. These data were used in Figure 11 to statistically determine the relationship between $\mathcal{E}_\varpi(\mathbb{E}_\parallel)$ (Scudder 2022a) and the mathematical location of $\mathcal{E}_=$, where equal contributions were observed from the primary thermal (core) and suprathermal (halo) components.

The column-normalized quantities were analyzed to extract the functional dependence of the variation indicated by the red line, reflecting

$$\overline{\mathcal{E}_=} \simeq \overline{\mathcal{E}_\varpi}(\varpi) + (4.16 \pm 0.48). \tag{16}$$
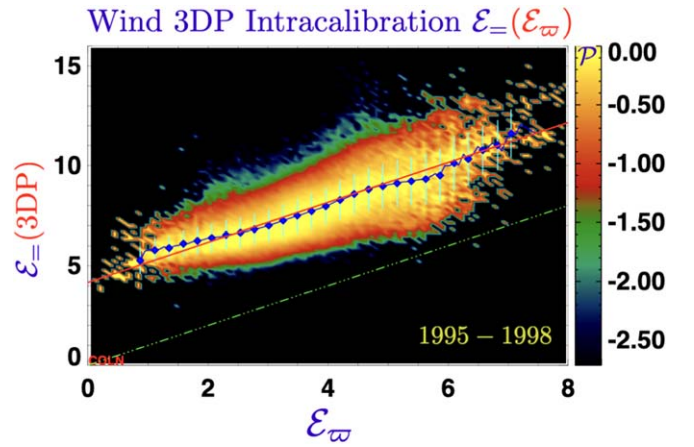
Figure 11. Evidence for the observed strong linear correlation between $\mathcal{E}_= = \mathcal{E}_\varpi + 4.16 \pm 0.48$ and summarizing $E_\parallel$ determinations (Scudder 2022a) and hinge-point locations from over 279,000 eVDF across 1995–1998, using the processed Wind data products (Salem et al. 2021) from the 3DP investigation (Lin et al. 1995).

This regression and the data clearly show that the hinge energy $\mathcal{E}_=$ depends on the size of $\mathcal{E}_\varpi$, which is determined by the size of $\mathbb{E}_\parallel$. At this level of modeling, the energy equivalent of this offset is constant in *local* thermal speed units across the Wind data set. At present, the size of this offset is a 4 yr empirical result used by SERM-II, with a possible interpretation discussed next.

9. Interpretation of $\mathcal{E}_\varpi < \mathcal{E}_=$

As mentioned above, Dreicer's inference of bifurcation is the result of simplifying the electron–electric field interaction by ignoring the velocity space diffusion, which generally grows for overdamped trajectories with increasing proximity to the separatrix identified and weakens with distance above the separatrix along underdamped trajectories. Thus the separatrix is permeable to the random walks allowed by the full Coulomb treatment.

Dreicer's analysis made approximations when identifying the minimum kinetic energy $\mathcal{E}_\varpi$ for runaway and the patterns in Figure 1 above. Omitted from that analysis was the description of diffusive scattering that is pivotal to predicting the actual rate of electrons migrating between the cyan and green integral curves identified by ignoring this process.

The experimental results from Figure 11 suggest than an energy gain in the range of $(3.68-4.64)kT_e$ is required to be transferred by the electric field to the fastest underdamped electrons before they are no longer distinguishable from the more pervasive underdamped electrons that arrive, staying on green integral curves from very large negative values of V_x. In this picture this corresponds to an increment of speed $\Delta v \simeq (1.16-1.37)\varpi$ that implies total speeds of $\nu_= \simeq (2.16-2.37)\varpi$. After achieving these speeds these emerging electrons at $\nu_=$ experience only 7%–9% of the weak friction they had overpowered when arriving at the separatrix from below.

It is likely that the spectral transition between $f(\mathcal{E}_\varpi)$ and $f(\mathcal{E}_=)$ in Figure 10 reflects the nearly complete dispersal and assimilation of those emerging underdamped electrons onto the runaway trajectories.

10. SERM-II Analysis with Hinge

In the wind's rest frame the even part of the overdamped part of the eVDF is assumed across all ν to have the form

$$f_c(\nu) = \alpha e^{-\nu^2}$$
$$\nu^2 = \frac{m_e v^2}{2kT_c} = \frac{E}{kT_c}$$
$$kT_c = -\left(\frac{d\ln f_c}{dE}\right)^{-1}. \qquad (17)$$

The even part across all ν of the underdamped component has the assumed form

$$f_h(\nu) = \beta e^{-(\nu\tau)^2}$$
$$\tau^2 \equiv \frac{T_c}{T_h}$$
$$kT_h = -\left(\frac{d\ln f_h}{dE}\right)^{-1}. \qquad (18)$$

At a dimensionless speed $\nu_=$ the cold and hot component have the same value:

$$f_c(\nu_=) = f_h(\nu_=) = \alpha e^{-\mathcal{E}_=}, \qquad (19)$$

determining the hot contribution with one less free constant:

$$f_h(\nu, \tau) = \alpha e^{-\mathcal{E}_=(1-\tau^2)-(\nu\tau)^2}. \qquad (20)$$

Dreicer's runaway density fraction δ involves

$$\delta = \frac{n_{\text{runaway}}}{n_e}, \qquad (21)$$

determined by Equation (12). Since the eVDF is a sum of two Gaussians, $\delta^{\text{Max}}(x)$ occurs twice in δ with different arguments x:

$$\delta^{\text{SERM}} = \frac{\tau^3 \delta^{\text{Max}}(\varpi) + e^{-\mathcal{E}_=(1-\tau^2)} \delta^{\text{Max}}(\varpi\tau)}{\tau^3 + e^{-\mathcal{E}_=(1-\tau^2)}}. \qquad (22)$$

The strahl does not participate in determining the runaway fraction δ^{3DP} since it has been shown (Scudder 2022a) to reside fully inside even the narrower separatrix determined by Fuchs et al. (1986).

For computational precision, the second term in the numerator of Equation (20) needs to be recast:

$$e^{(-\mathcal{E}_=(1-\tau^2))} \delta^{\text{Max}}(\varpi\tau) = e^{(-\mathcal{E}_=(1-\tau^2)-\varpi^2\tau^2)} \mathcal{G}(\varpi\tau)$$
$$\mathcal{G}(Y) \equiv \frac{2Y}{\sqrt{\pi}} + (1 - 2Y^2)\text{erfcx}(Y)$$
$$\text{erfcx}(u) \equiv e^{u^2}\,\text{erfc}(u)$$
$$H_o \equiv \mathcal{E}_= - \mathcal{E}_\varpi \simeq 4.16 \pm 0.48, \qquad (23)$$
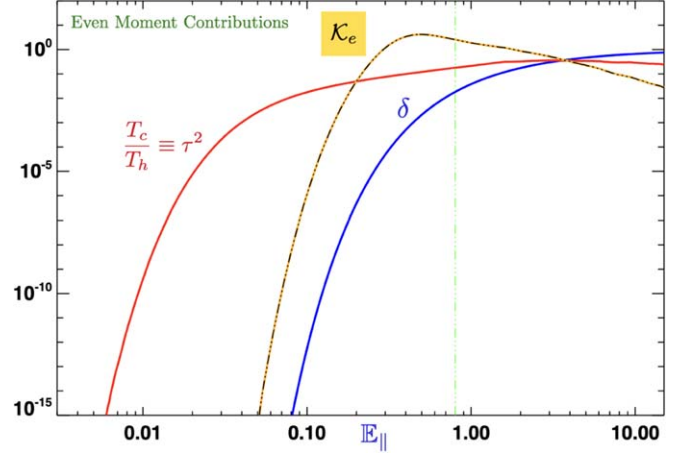
yielding

$$e^{(-\mathcal{E}_=(1-\tau^2))} \delta^{\text{Max}}(\varpi\tau) = e^{(H_o\tau^2-\mathcal{E}_=)} \mathcal{G}(\varpi\tau). \qquad (24)$$

Given the calibration curve (Equation (14)) for $\delta^*(\varpi)$, the SERM value for $\tau(\varpi)$ is determined implicitly by

$$\delta^{\text{SERM}}(\varpi, \mathcal{E}_=^{\text{Model}}(\varpi), \tau(\varpi))) = \delta^{\text{Max}}(\varpi)^{0.893}, \qquad (25)$$

Figure 12. 1:1 functional dependence of $\{\mathcal{K}_e, \tau, \delta\}$ on $\mathbb{E}_\parallel$. The SERM contributions to $\mathcal{K}_e$ shown here will be modified further when SERM odd-moment signatures are included. A useful connection to other observables is the relationship $\mathbb{E}_\parallel \simeq \mathbb{K}_{P_e}/2$, where $\mathbb{K}_{P_e}$ is the mean free path for the thermal-speed electron in units of the electron pressure gradient scale, also known as the *pressure Knudsen number.*

provided Equation (16) replaces $\mathcal{E}_=$ with the documented dependence on ϖ; that is,

$$\delta^{\text{SERM}}(\varpi, \tau) = \frac{\tau^3 \delta^{\text{Max}}(\varpi) + e^{(H_o\tau^2-\mathcal{E}_=(\varpi))} \mathcal{G}(\varpi\tau)}{\tau^3 + e^{-\mathcal{E}_=(1-\tau^2)}}. \qquad (26)$$

## 11. Inferring SERM-II eVDF from Fluid Variables

Upon solving Equation (26) (and showing uniqueness) a correspondence exists between the even electron fluid moments and the local shape parameter characterizations of the SERM-II eVDF, and finally the shape factors of the two Gaussian subcomponents of the nonthermal eVDF:

$$\{n_e, U_{e,\parallel}, P_e, \mathbb{E}_\parallel\} \rightarrow$$
$$\{\varpi, \delta, \tau, \mathcal{E}_=, \mathcal{K}_e\} \rightarrow \{n_c, n_h, T_c, \mathcal{T}_h\}. \qquad (27)$$

Typically solutions must be found for an allowable uncertainty spread of $\mathcal{E}_=$, shown in Figure 11; when these solutions are averaged the cited best expectation, τ, is the defined average. The variances across these estimates are used to form the indicated error bars about τ, trace indicated in Figure 13 below.

These newly found 1:1 SERM constitutive relations for δ, τ, and $\mathcal{K}_e$ with $\mathbb{E}_\parallel$ are illustrated across a broad range of expected values in Figure 12 and at higher resolution in Figure 13. These relationships will be referred to as SERM constitutive relationships. Clearly the SERM-I and SERM-II eVDF solutions are leptokurtic ($\tau \lesssim 1$) and by construction are compatible with Coulomb collisions and Dreicer's insight via the local size of $\mathbb{E}_\parallel$. SERM-II estimates include the refinement of a hinge point at its statistically observed location $\mathcal{E}(\varpi)_=$, above the minimum runaway boundary of $\mathcal{E}_\varpi$.

By eliminating the $\mathbb{E}_\parallel$ dependence, correlations between SERM-II shape variable pairs can be inferred. These correlated shape pairs imply correlations between the eVDF's reported fit shape parameters that have long been known (see Figure 4) in solar wind observations, but were only provided with their first explanation with SERM-I (Scudder 2019c).
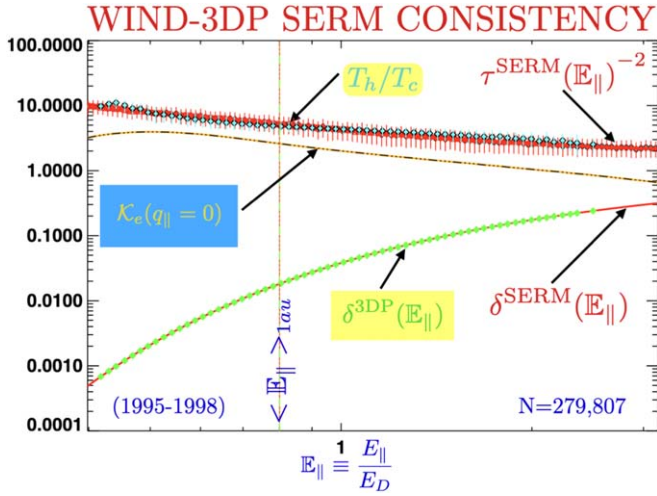
Figure 13. Documentation of Dreicer bifurcation of the observed solar wind eVDF in the measured solar wind $E_\parallel$. This SERM-II 4 yr Wind-3DP data comparison conclusively documents the detection of Dreicer's bifurcation by plasma runaway in the solar wind's observed $E_\parallel$.

To solidify the quality of the SERM-II model's precision, a magnified portion of Figure 12, presented in Figure 13, illustrates the nearly perfect correspondence between (i) underlying red curves for SERM-II theoretical parameters versus newly measured $\mathbb{E}_\parallel$ and the superposed (ii) statistical summaries of the same properties from Wind-3DP data indicated by cyan dots for $\mathcal{T}_h/T_c$ and green dots for Dreicer's runaway density fraction, δ^{3DP}.

Because the reasons for $E_\parallel \neq 0$ are as generic as the conditions of astrophysics, the in situ documentation of Figure 13 is a strong argument that such behavior is expected to occur in virtually all fully ionized astrophysical plasmas.

12. $\{\varpi, \delta, \tau, \mathcal{E}_=, \mathcal{K}_E, P_E, N_E\} \rightarrow (N_C, N_H, T_C, \mathcal{T}_H)$

Given an electron fluid characterization, the present SERM-II model allows one to suggest the even moments of the requisite eVDF in terms of two superposed Gaussian distributions, thus completing the last stage in Equation (27). This approach gives a likely nonthermal eVDF consistent with quasi-neutrality, the Coulomb cross section, and the modeled fluid's moment behavior.

SERM-II applications in this vein (i) could be determined from empirical suggestions of remote fluid properties or the output of fluid solutions for the plasma at the two-fluid level. Those of the second type would allow (ii) conducting a complete justification of closure (see Scudder 2019b) that could validate or contradict the approximations made to produce closures used to truncate the infinite set of equations required to formally replicate the kinetic equation.

Either focus requires estimating $\mathbb{E}_\parallel$ where the fluid moments are known. Knowing fluid spatial profiles, this may be done using the electron momentum equation. If the moments are known only in isolated locations the little used, but well known, relationship between $\mathbb{E}_\parallel$ and the pressure Knudsen number (see Equation (2) of Scudder 2019a) can provide the necessary estimate. In either instance estimating $\mathbb{E}_\parallel$ determines $\mathcal{E}_\varpi$, which constrains $\mathcal{E}_=$ using Equation (16). Together, all of these relations allow estimates of δ and τ to be inferred by interpolating their traces as functions of $\mathbb{E}_\parallel(r)$, shown in Figure 12.

12.1. SERM's Nonthermal Subcomponents' Shapes from Electron Fluid Variables

With the knowledge of $\tau(\mathbb{E}_\parallel(r))$ the free parameters of SERM-II's two isotropic Gaussian subcomponents for the underlying eVDF can be determined using

$$\frac{n_c}{n_e} = \frac{\tau^3}{\tau^3 + \exp(-\mathcal{E}_=(\varpi)(1 - \tau^2))}$$
$$\frac{n_h}{n_e} \equiv \frac{\exp(-\mathcal{E}_=(\varpi)(1 - \tau^2))}{\tau^3 + \exp(-\mathcal{E}_=(\varpi)(1 - \tau^2))} \quad (28)$$

and Equation (29) below.

When $\tau \downarrow 0$ the halo density fraction is 100%, but when $\tau \uparrow 1$ the core *and* halo fraction approach 0.5, since in this regime the superposed core and halo are identical, each contributing half the total density. This regime is hardly ever expected since it requires $\mathbb{E}_\parallel = 0$, which is virtually impossible in the inhomogeneous plasmas of astrophysics.

The runaway density fraction, δ, is *not* determined by knowing both n_h and n_c, but is available from the calibration curve in Figures 12 and 13, once $\mathbb{E}_\parallel$ is available.

The thermal and suprathermal temperatures of the form $(-dE/dlnf)$ are constrained by the total pressure, P_e, to be determined as

$$k_B T_h = \frac{P_e}{n_h + n_c \tau^2}$$
$$k_B T_c = \frac{P_e \tau^2}{n_h + n_c \tau^2}$$
$$\frac{T_c}{T_h} = \tau^2. \quad (29)$$

The ratio of partial pressures of the two components is

$$\frac{P_h}{P_c} = \frac{n_h}{n_c \tau^2}$$
$$= \frac{exp(-\mathcal{E}_=(\varpi)(1 - \tau^2))}{\tau^5}. \quad (30)$$

Equations (28) and (29) provide sufficient information to make an even two-Gaussian mathematical model of the suggested eVDF compatible with the input two-fluid moments, Coulomb cross section, and quasi-neutrality. SERM-II does not yet support a heat flux, but it will soon (J. D. Scudder 2023, in preparation).

These equations represent SERM-II's *deconstruction* of the two-fluid moment profiles, producing a positive definite, nonthermal eVDF containing zeroth, second and fourth moments, and all even moments. These leptokurtic distributions have the same total density and electron pressure as implied by the fluid model.

12.2. Inferring the eVDF for the Two-fluid Solar Wind Model

As an example of SERM's application, the two-fluid profiles of solar wind density, electron pressure, and flow speed are reproduced in Figure 14 from digital files shared by Chandran et al. (2011). The solar wind solution incorporated a low-frequency treatment of reflection-driven, Alfvén-wave-turbulent, dual-energy equations closed by a two-zone heat-flow closure for electrons, ion heat-flux closure, and ion anisotropy limiters based on collisionless kinetic theory.
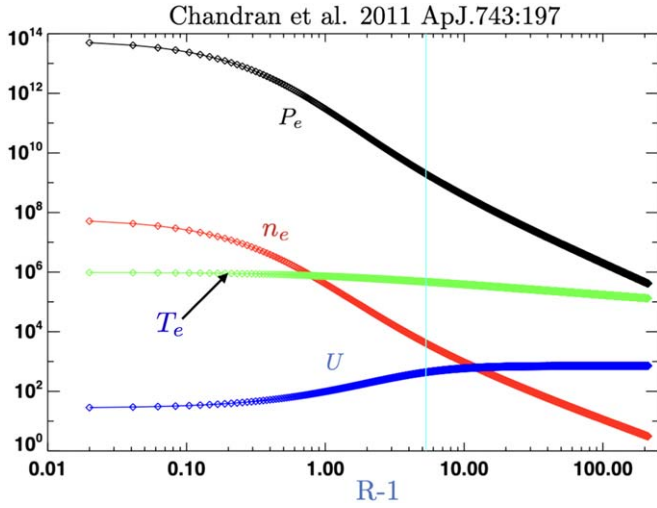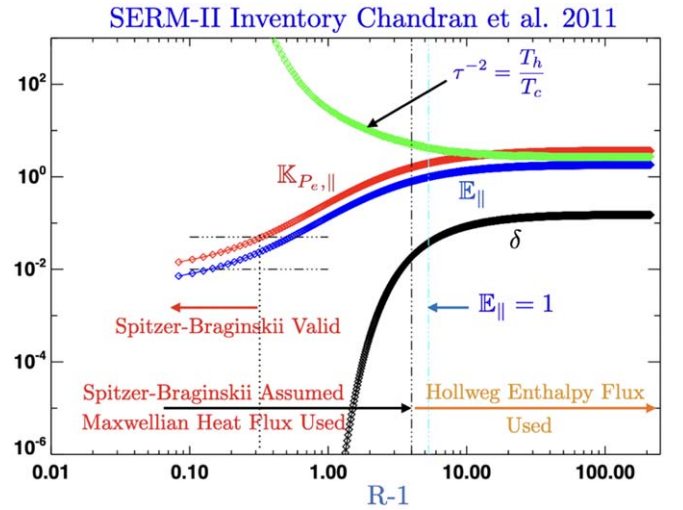
Figure 14. Profiles of electron pressure $P_e(r)$, density $n_e(r)$, and flow speed U (r) from a two-fluid Alfvén-wave-driven high-speed solar wind model (Chandran et al. 2011). Alfvén point reported at the location of the vertical cyan line.

Figure 15. Inferred radial variation of $\mathbb{E}_\parallel$, (blue), $\mathbb{K}_{P_e}$ (red), δ (black), and τ^{-2} (green) using the SERM-II model, unpacking the information of the two-fluid variations of the published two-fluid solar wind model of Chandran et al. (2011). The height of the point of observation above the nominal solar surface is the abscissa, $H = R - 1$, where R is the radial distance to the point.

The solution's inferred radial profiles for $\mathbb{E}_\parallel(r)$ are shown using the electron momentum equation and the SERM eVDF constituitive relations, $[\delta(\mathbb{E}_\parallel(r)), \tau^{-2}(\mathbb{E}_\parallel(r))]$, obtained from Figure 12 by interpolation.

Near the coronal base at $H \simeq 0.01\,R_\odot$ $\mathbb{E}_\parallel < 0.01$ is small, implying the ion collisional drag deceleration there on a thermal-speed electron was much larger than the electron acceleration by $E_\parallel$. In this locale SERM-II predicts only a very weak, off-scale, density fraction of runaways, δ. In this regime the very small density of suprathermal electrons has a very high effective slope temperature. The partial pressure in this sparse hot component rises nine orders of magnitude between 1.08–5 $R_\odot$. $\mathbb{E}_\parallel$ increases rapidly with increasing radius, surpassing $\mathbb{E}_\parallel = 0.1$ by $R = 2\,R_\odot$ and unity by $6\,R_\odot$. This variation of $\mathbb{E}_\parallel(r)$ signals the systematic role reversal *for the thermal-speed electron* between being heavily overdamped at low altitudes, approaching underdamped status. Across this same radial range the hinge point of the leptokurtic eVDF moves down from $34kT_e$ to $9kT_e$ and the runaway boundary lowers from $30kT_e$ down to $5kT_e$. From Figure 10 the phase-space diffusive transition layer for the eVDF between $\mathcal{E}_\varpi$ and $\mathcal{E}_=$ raises the fraction of the distribution available to support the skew for the heat flux. These estimates suggest the fractional population of nonthermal electrons just above the separatrix are being strongly enhanced across this transition. This is the radial zone where wind acceleration is strongest, but is still below the solution's Alfvén point. Across this region Chandran et al. (2011) are using the Spitzer–Braginskii heat closure, which assumes the eVDF is perturbatively related to a Maxwellian.

Though finite at $r = 1.01\,R_\odot$, the halo-to-core density fraction δ rises sharply by more than *10 orders of magnitude* across the narrow radial range 1.08–6 $R_\odot$, where $\mathbb{E}_\parallel$ increases from 0.1 to 1. The runaway fraction δ rises to nearly 5% by $R = 6$, smoothly continuing to rise toward still higher values (30%–40%) reported by Wind 3DP at 1 au. This strong increase in halo density fraction occurs where the suprathermals are suggested to have slope temperatures nearly $10\times$ that of the overdamped thermal electrons.

The enhanced density fraction in runaway, accompanied by coordinated suprathermal partial pressure changes (see

Figure 16. Radial profile of solar wind speed (green), density fraction in runaway δ (cyan), and electron excess kurtosis $\mathcal{K}_e$ (red). A broad development is shown of radially increasing $\mathbb{E}_\parallel$, δ, and $\mathcal{K}_e$. A strong onset of nonthermal signatures is seen when $0.1 \leqslant \mathbb{E}_\parallel \leqslant 1$, during the bulk speed U's acceleration, but well inside the indicated Alfvén point, R_A.

Figures 13 and 15) cause the fourth moment of excess electron kurtosis $\mathcal{K}_e$ to increase strongly across this same region of the inner heliosphere shown, as shown in Figure 16.

12.3. Inner Heliosphere's Radial Gradient of Kurtosis

Figure 16 provides an initial view of the rapidly varying kinetic changes SERM-II would imply for the inner heliosphere. The input for the calculation are the two-fluid profiles for P_e, n_e, and U from a two-fluid solar wind solution (Chandran et al. 2011). These profiles smoothly connect the accepted coronal boundary condition to 1 au conditions typical for a $700+$ km s^{-1} solar wind.

The solar wind expansion above the coronal base is typified by radially monotonic growth of (i) solar wind speed, (ii) $\mathbb{E}_\parallel$, (iii) δ, (iv) excess kurtosis $\mathcal{K}_e$, and (v) decay of suprathermal to thermal slope temperature ratio, τ^{-2}. Above $r \simeq 4\,R_\odot$ $\mathcal{K}_e$ is surprisingly very nearly the same size as $\mathbb{E}_\parallel$, with both already

considered nonperturbative and large. When directly measured near 1 au these variables show this same strongly correlated behavior and nonperturbative size as seen in the Wind data (see Figure 2).

Observations of the eVDF at 1 au since 1968 have shown omnipresent excess kurtosis, $\mathcal{K}_e$. The rapid statistical physics transformation suggested by this fluid solution from Gaussian forms below $R \simeq 2\,R_\odot$ to strongly kurtotic eVDF well below the sonic or Alfvén point $6\,R_\odot$ is totally new. The rapid growth of excess kurtosis occurs astride the dominant zone where the solution's wind vigorously accelerates inside the Alfvén point. This kurtosis has been reported by the Parker Solar Probe (PSP) down to the lowest radius achieved. Unfortunately, the new suggestions of this paper are for the domain below the PSP's minimum perihelion of $\simeq 9\,R_\odot$.

In situ model-independent heat-flow observations in the solar wind are dominated by the pear-shaped, skewed asymmetry of the phase space at suprathermal energies; the magnitude of the heat flow varies directly as the number of charge carriers available to transport the energy asymmetry. The suggested strong variation of the excess kurtosis below the Alfvén point appears to suggest that the radial variation of this kurtosis could impact the divergence of the heat flows that do occur.

The fluid equations solved to obtain this model's profiles were totally unaware of the role of electron kurtosis or the strong transformation of the kinetic character just suggested by SERM. The modeled two-fluid equations were closed at the third-moment level involving the heat flux; when formulated the heat-flux model adopted was known to be inappropriate. Its use provided a *rationale* for closing the infinite set of equations, despite avoiding a justification for their suitability. While the solution emphasized the role of Alfvénic acceleration of the wind, it had incorporated a Spitzer–Braginskii (Spitzer & Härm 1953; Braginskii 1965) heat-flow closure to make this study at the fluid level. As used, this closure involved relying on an eVDF that possessed negative phase-space probabilities (eVDF < 0; see Scudder 2021). The interval of this defect is shown in Figure 15. The modeled heat flux used to truncate the fluid equations was not adequate either (i) to truncate the moments of the kinetic equation, or (ii) or evaluate whether physically described heat flow could be important for understanding the solar wind expansion. As further support for this argument, the strong onset of kurtosis suggested by SERM occurs across the same radial domain where Spitzer's heat law was used beyond its validity (see Figures 15 and 16).

13. Discussion and Conclusion

The fidelity of SERM-II's prediction of ambient wind properties over a 4 yr data set has been demonstrated in this paper. By virtue of passing these tests SERM's primary thesis of the role of Dreicer runaway physics in the solar wind is strongly supported.

The suggestions of SERM as developed by the end of this paper is that the lowest-order eVDF for the plasma supporting the observed solar wind profiles must be leptokurtic since $E_\parallel$ is always required to make the solar wind expansion quasi-neutral.

This paper has also documented 4 yr of empirical support for the SERM model's accuracy when partitioning the electron fluid's pressure and density between thermal and suprathermal components.

Quantitative evidence has been supplied that a steady variant of Dreicer's runaway physics is the causal agent of the ubiquitous leptokurtic eVDFs that have now been measured in the solar wind for 54 yr and only recently explained with SERM (Scudder 2019c).

These findings represent striking and promising departures from the traditional theoretical assumptions that attempt to model the observed solar wind eVDF as a perturbatively modified Maxwellian that alone has zero excess kurtosis and transports no heat.

The heat-flow moment depends on the skewness of the eVDF; observationally, the skewness depends directly on the density of heat carriers and the distribution of heat energy transported. Observed eVDFs with model-independent assays of the heat flow demonstrate that the density of heat carriers and heat energy moved are predominantly supported by the nonperturbative, nonthermal part of the leptokurtic eVDF.

The much needed and overdue improvement in the heat laws used for modeling the solar plasmas must provide a nonperturbative recipe both for (i) the promotion of part of the plasma to be nonthermal, and (ii) for the skewed energy support of the heat that flows.

This paper has shown the SERM-II model is fully capable of suggesting the rationale for this first improvement. The sequel (J. D. Scudder 2023, in preparation) will discuss surmounting the second hurdle by producing a nonperturbative formulation for the plasma heat law that incorporates the work of Dreicer and SERM-II.

Appendix A
Wind 3DP Characterization of Electron eVDF

The Wind 3DP electron data have been processed both as a model-independent 3D eVDF and as a superposition of three modeled subcomponents: a low-energy-range convected
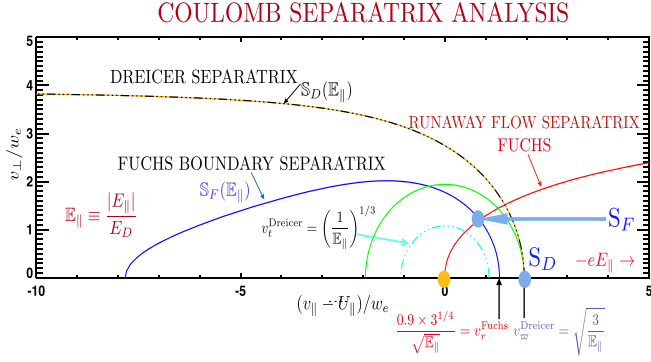
Figure 17. Labeled boundaries in hydrogenic plasma with the same $\mathbb{E}_{\parallel}$ for (i) Dreicer (1960) and (ii) Fuchs et al. (1986) integral curves considering $E_{\parallel}$ with (i) ion drag only, and (ii) ion drag and energy loss. Both show two intersecting separatrices: (i) $v_{\perp} = 0$ and yellow–black dotted parabola, (ii) blue pear-shaped curve and red curve rising from $|\mathbf{v}| = 0$. Both models show (a) a node in integral curves at $|\mathbf{v}| = 0$, and (b) saddle points where separatrices intersect, S_D and S_F. Topologically the integral curves of both models are the same, despite relocation of the saddle point.

bi-Maxwellian, usually called the *core*, a higher-energy convected bi-kappa distribution, called the *halo*, and a characterization of data not well fit by these two best fits that is the basis for the *strahl* characterization (see Salem et al. 2021). These separate components are modeled in super-position and given their own velocity space moments described in the ion frame of reference, having inertial velocity $\mathbf{U}$. As the strahl is a modest, but highly angular, augmentation of the core population along the heat-flux direction of the magnetic field, the core and halo eVDFs are the principal determinants of the nonthermal even-moment properties of the electrons.

Since the core and halo populations are rarely very anisotropic, all temperature moments used when applying SERM-II come from one-third the trace of the gyrotropic quantities.

Although well known, much of the modeled halo in the superposed eVDF resides in the core low-energy range. Thus integral properties like the halo fit density are higher than the density of halo component electrons outside the energies where the modeled core dominates the composite eVDF. Further, neither of these quantities is the density of electrons involved in the Dreicer runaway that are computed for this paper.

A similar issue pertains to the halo temperature. As usually reported, it is the mean proper frame energy averaged over all speeds for the halo fit. It is not the mean energy of those suprathermal electrons found outside the domain dominated by the core fit. For the considerations below the best-fit observed kappa distribution is sampled for this paper above the runaway threshold and assigned a best-fit $\mathcal{T}_h$ from a fit of these phase-space readings to a Maxwellian across the suprathermal domain. This characterization is for the purposes of comparison with the SERM model, which at the present level of development (SERM-II in this paper) assumes a superposition in the ion rest frame of two nondrifting Gaussians supporting the nonthermal distribution that dominate the eVDF density and partial pressures. This will be improved in a subsequent development that addresses odd moments.

Appendix B
Fuchs et al. (1986) Updated Description of Runaway

Several decades later, Fuchs et al. (1986) made a more complete investigation of the runaway bifurcation illustrated in Figure 17. For clarity the integral curves have been omitted. This figure shows both the separatrices (yellow with black dashes) according to Dreicer's formulation and the richer separatrix structure found by Fuchs et al. (1986). Dreicer's formulation only tracked the impact on the integral curves of ion energy loss and electric acceleration.

Fuchs et al. (1986) incorporated energy loss for electrons in a form that was faithful for this exchange when it occurred in the nominally runaway regime. Their analysis showed two important changes: (i) the tear-dropped blue separatrix, which is the analog of Dreicer's parabola, is now totally bounded; (ii) a second red separatrix occurs crossing the blue separatrix at a saddle point S_F. The integral curves have the same topology as Dreicer.

The analogues of Dreicer's cyan integral curves circulate within the blue separatrix; when starting to the left of the red separatix the circulation peaks along the red separatrix and is then guided toward the origin. The integral curves starting to the right of the red separatrix (but still within the blue separatrix) produce a counterclockwise circulation peaking along the red separatrix below the saddle point S_F and then converging back on the origin.

The analogues of Dreicer's green integral curves start at large negative V_x *outside* the blue separatrix; when approaching the red separatrix the integral curves are deflected to flow *along but outside of* the red separatrix. An apparently distinct group of integral curves start at $V_x > 0$. For $V_x < \varpi$ these curves initially decelerate in V_x but have a growing V_y. These curves approach the red separatrix from below and are then guided by the red separatrix to large V_x. Stream lines with initial coordinates $V_x \geqslant \varpi$, $V_y = 0$ rise toward the red separatrix without decelerating; approaching the red separatrix the level curves are then guided to very large V_x. Sketches of these integral curves can be found in Fuchs et al. (1986).

The topology of Fuchs et al. and Dreicer are analogous. The underdamped curves circulate through the origin. They remain separated from those that start outside the inner separatrix that now have two different V_x sites of origin. The analogy is perhaps seen better by realizing that in Dreicer the red $V_x > \varpi$, $V_y = 0$ segment in Figure 1 is the analog of the included red separatrix in Fuchs et al. (1986) *above* the saddle point at S_F. In both models the runaway integral curves are guided to be asymptotically parallel to this ray/curve.

Appendix C
Full Dreicer Formulae

Dreicer's variables and abbreviations used in the text are fully defined here in terms of customary CGS variables. The variable E_D used in this paper and E_c by Dreicer (1959, 1960) are identical. The $ln\Lambda$ expression alone is written in terms of temperature $\mathbb{T}_e$ in eV units rather than in CGS units, which is

indicated elsewhere by T_e:

$$w_e \equiv \sqrt{2kT_e/m_e}$$

$$ln\Lambda_c^{e-i} = \frac{47}{2} + ln[\mathbb{T}_e^{\frac{5}{4}} n_e^{-\frac{1}{2}}]$$

$$- \frac{1}{2}\sqrt{(-1 + ln\mathbb{T}_e^{\frac{1}{2}})^2 + 10^{-5}}$$

$$\equiv ln\Lambda$$

$$\lambda_{\mathrm{mfp}}(w_e, i) \equiv \frac{(kT_e)^2}{\pi \, n_e \, e^4 \, ln\Lambda} \equiv \lambda_{\mathrm{mfp}}$$

$$\nu_{ei}(w_e) \equiv w_e/\lambda_{\mathrm{mfp}} \equiv \nu_{ei}$$

$$E_c \equiv E_D$$

$$|e|E_D \equiv m_e w_e \nu_{ei} = \frac{2kT_e}{\lambda_{\mathrm{mfp}}}$$

$$= \frac{2\pi n_e e^4 ln\Lambda}{kT_e} \propto \frac{n_e}{T_e}. \tag{C1}$$

The form above for $ln\Lambda_c^{e-i} \equiv ln\Lambda$ provides a continuous formula across the quantum-mechanical regime, $\mathbb{T}_e \simeq 10$ eV, and represents an essentially equivalent form to two separate equations (Fitzpatrick 2015, Equation (3.124); also Spitzer 1967) needed for solar wind plasmas.

ORCID iDs

Jack D. Scudder ⬤ https://orcid.org/0000-0001-7975-5630

References

Braginskii, S. I. 1965, RvPP, 1, 205
Chandran, B. G. D., Dennis, T. J., Quataert, E., & Bale, S. D. 2011, ApJ, 743, 197
Dreicer, H. 1959, PhRv, 115, 238
Dreicer, H. 1960, PhRv, 117, 329
Feldman, W. C., Asbridge, J. R., Bame, S. J., Montgomery, M. D., & Gary, S. P. 1975, JGR, 80, 4181
Fitzpatrick, R. 2015, Plasma Physics, An Introduction (Boca Raton, FL: CRC Press), 64
Fuchs, V., Cairns, R. A., Lashmore-Davies, C. N., & Shoucri, M. M. 1986, PhFl, 29, 2931
Landi, S., & Pantellini, F. G. E. 2001, A&A, 372, 686
Lin, R. P., Anderson, K. A., Ashford, S., et al. 1995, SSRv, 71, 125
Maksimovic, M., Pierrard, V., & Lemaire, J. 1997, A&A, 32J, 725
Montgomery, M. D., Bame, S. J., & Hundhausen, A. J. 1968, JGR, 73, 4999
Olbert, S. 1983, JPL Solar Wind Five (SEE N84-13067 03-92), 149
Parker, E. N. 1958, ApJ, 128, 677
Salem, C. S., Pulupa, M., Bale, S. D., & Verscharen, D. 2021, arXiv:2107.08125
Scudder, J. D., & Olbert, S. 1979a, JGR, 84, 2755
Scudder, J. D., & Olbert, S. 1979b, JGR, 84, 6603
Scudder, J. D. 1992b, ApJ, 398, 318
Scudder, J. D. 1992c, in Solar Wind Seven, ed. E. Marsch & R. Schwenn (Amsterdam: Elsevier), 103
Scudder, J. D. 1996, JGR, 101, 13461
Scudder, J. D. 2019a, ApJ, 882, 146
Scudder, J. D. 2019b, ApJ, 885, 148
Scudder, J. D. 2019c, ApJ, 885, 138
Scudder, J. D. 2021, ApJ, 907, 90
Scudder, J. D. 2022a, ApJ, 934, 151
Spitzer, L., & Härm, R. 1953, PhRv, 89, 977
Spitzer, L. J. 1967, Physics of Fully Ionized Gases (2nd ed.; New York: Wiley Interscience)
Zouganelis, I., Maksimovic, M., Meyer-Vernet, N., et al. 2004, ApJL, 606, 542